



# Top–Down Approach for the Deposition of Photoactive (Na<sub>0.5</sub>Bi<sub>0.5</sub>)TiO<sub>3</sub>-Based Heterojunctions by Flame Spray: Analysis of Deposition Parameters

A. I. Gutiérrez-Pérez<sup>1</sup> · M. T. Ayala-Ayala<sup>1,2</sup> · A. G. Mora-García<sup>1</sup> · C. Hernández-Navarro<sup>1,4</sup> · S. Pérez<sup>1</sup> · J. A. Díaz-Real<sup>3</sup> · J. González Hernández<sup>1</sup> · J. Muñoz-Saldaña<sup>1</sup>

Submitted: 1 October 2022 / in revised form: 23 May 2023 / Accepted: 17 June 2023 / Published online: 6 July 2023  
© ASM International 2023

**Abstract** Visible-light photoactive (Na<sub>0.5</sub>Bi<sub>0.5</sub>)TiO<sub>3</sub> (NBT)-based heterojunctions have demonstrated their applicability in environmental remediation. The photocatalytic properties of NBT-based coatings are here reported. NBT-based materials were deposited by oxyacetylene flame spray (FS). The physicochemical properties were analyzed as a function of the spraying parameters: fuel/oxygen ratio (F/O), stand-off distance (SOD), and total gas flow (TF). A flame with reducing characteristics promotes the formation of TiO<sub>2</sub> (anatase and rutile) and Bi<sub>4</sub>Ti<sub>3</sub>O<sub>12</sub>, while an oxidizing flame results in coatings rich in NBT and Bi<sub>4</sub>Ti<sub>3</sub>O<sub>12</sub>. The SOD mainly influences the degree of crystallinity, which is higher at shorter distances. Optical

properties estimated by UV–VIS diffuse reflectance confirmed an increase in light absorption after the FS process, with an  $E_g$  red shift from 3.32 eV of the NBT powder to 2.63–2.96 eV of the coatings. These values are dependent on the F/O, with a significant  $E_g$  narrowing under reducing conditions. Photoelectrochemical measurements revealed that faster electron collection is obtained due to the transformations occurring throughout the FS process while still retaining nearly 70 and 88% of the photocurrent density ( $j_{ph}$ ) at UV and visible light, respectively. These results suggest the great potential of the FS methodology to produce multiphase photocatalytic coatings by tuning the processing parameters.

**Keywords** bismuth-based heterojunctions · ceramics · flame spray · sodium bismuth titanate · thick coatings · visible-light photoactive

This article is part of a special topical focus in the *Journal of Thermal Spray Technology* on New and Emerging Markets in Thermal Spray. The issue was organized by Dr. Andrew Vackel, Sandia National Laboratories; Dr. John Koppes, TST Engineered Coating Solutions; Prof. Bertrand Jodoin, University of Ottawa; Dr. Dheepa Srinivasan, Pratt and Whitney; and Prof. Shrikant Joshi, University West.

✉ J. Muñoz-Saldaña  
jmunoz@cinvestav.mx

<sup>1</sup> Laboratorio Nacional de Proyección Térmica, CENAPROT, Centro de Investigación y de Estudios Avanzados del IPN, Lib. Norponiente 2000, Fracc. Real de Juriquilla, 76230 Querétaro, QRO, Mexico

<sup>2</sup> Institut für Technische Chemie, Gottfried Wilhelm Leibniz Universität Hannover, Callinstrasse 3, 30167 Hannover, Germany

<sup>3</sup> Centro de Investigación y Desarrollo Tecnológico en Electroquímica, CIDETEQ, Parque Tecnológico S/N, Sanfandila, 76703 Pedro Escobedo, QRO, Mexico

<sup>4</sup> Tecnológico Nacional de México CRODE-Celaya, Manuel Orozco I. Berra 92, Col. Residencial Tecnológico, 38010 Celaya, Guanajuato, Mexico

## Introduction

Nowadays, enormous industrialization and consumption of natural resources are causing the world to face problems that require urgent attention, including environmental protection and remediation, along with the storage and conversion of alternative energies (Ref 1–3). Air and water pollution are harmful and pose a higher risk to life. In this regard, photocatalysis has emerged as an environmentally friendly, low-cost, and non-toxic technology for the mineralization of recalcitrant hazardous pollutants (Ref 4). For this purpose, semiconductor oxides such as TiO<sub>2</sub>, ZnO, WO<sub>3</sub>, and perovskites (ABO<sub>3</sub>) have been used as highly efficient photocatalysts for pollutant removal (Ref 5).

Semiconductor design and selection are critical to achieve efficient photocatalytic performance. A

semiconductor must possess desirable physical and chemical properties such as a high density of charge carriers (n-type or p-type semiconductors), and the conduction and valence band edge potentials ( $E_{CB}$  and  $E_{VB}$ , respectively) must be adequate to carry out the photocatalytic degradation reactions. In a photocatalytic reaction, a semiconductor is irradiated by light with a wavelength equal to or higher than its  $E_g$ , exciting electrons ( $e^-$ ) from the valence band (VB) to the conduction band (CB), leaving behind holes ( $h^+$ ). These photogenerated charge carriers migrate to the semiconductor surface and directly or indirectly take part in redox reactions (Ref 6). In this regard, it is desirable that charge recombination be suppressed, allowing their availability to participate in the reactions, and finally, it is favorable that the optical absorbance be extended to the visible (VIS) and near-infrared (NIR) regions of the sunlight to harness photons from the major portion of the solar spectrum. Some of the strategies for the development and design of efficient photocatalysts include tuning the band gap (introducing structural dopants or defects) and the formation of heterojunctions by coupling two semiconductors with appropriate band positions to improve charge separation and transfer as well as to reduce recombination rates (Ref 7).

Bismuth-based oxide semiconductors have received considerable attention as potential photocatalysts due to their structural characteristics. In the  $(\text{Na}_{0.5}\text{Bi}_{0.5})\text{TiO}_3$  (NBT) perovskite, hybridization of the orbitals O  $2p$  and Bi  $6s$  in the valence band and the high dispersion Bi  $6s$  orbital in the electronic structure is reported to increase the mobility of photogenerated charge carriers, decrease the band gap, and extend the visible-light response (Ref 8). The covalent–ionic type bonding between Bi and O is expected as  $\text{Bi}^{3+}$  shows lone pair  $6s$  effect (Ref 9). In addition, the crystal structure of titanates constructed by a sheet of edge- and/or corner-sharing  $\text{TiO}_6$  octahedra forming zigzag ribbon or tunnel structures is suitable for the accommodation of the catalytic active phases to raise the efficiency of the separation of photoexcited charges (Ref 10).

Perovskites based on NBT are a family of lead-free piezoelectric ceramics (Ref 11) that have excellent photocatalytic properties for wastewater treatment (Ref 12). In addition, NBT ceramics present cost-effective fabrication conditions because they can be synthesized by mixed oxide powders, high-energy ball milling, and solid-state reaction (SSR) (Ref 13, 14). Pure NBT is a semiconductor with an optical bandgap of around 3.2 eV, so it can only be activated under UV light, which limits its functional application in sunlight conditions.

Recently, it has been reported that the sintering process (Ref 15) of spray-dried microspheres (Ref 16) reduces the optical bandgap of pure NBT powder synthesized by SSR

from 3.23 to 3.08 eV, and the flame-sprayed coating process reduces it to 1.93 eV. Therefore, NBT prepared in powder form or as a coating is potentially a UV–vis-active catalyst for environmental remediation. However, only a few studies have demonstrated the photocatalytic activity of NBT. As mentioned before, an effective strategy to enhance the photocatalytic activity of a UV-active catalyst and carry out the desired redox reactions is by engineering the coupling of semiconductors into heterojunctions that assemble two or more catalysts (Ref 17). A properly functioning heterojunction exhibits efficient charge carrier separation, transfer, and reaction phenomena. As already reported, the energy levels must be staggered, and the catalyst with a higher  $E_{CB}$  must be capable to be a photoactive semiconductor in visible light driven to inject electrons into the CB of the other semiconductor (Ref 18). Some studies have reported the activity of NBT assembled in heterojunction with  $\text{TiO}_2$  (Ref 19) or  $\text{Bi}_2\text{O}_3$  (Ref 20, 21). For instance, the  $\beta\text{-Bi}_2\text{O}_3/\text{NBT}$  heterojunction, which is active in visible light and has remarkable efficiency for methanol photooxidation, was prepared by high-energy ball milling. The authors reported a red shift in the light absorbance of NBT heterojunctions and an enhanced performance of their photocatalytic activity due to the staggered band alignment that enables the mobility of charge carriers (Ref 21).

An interesting photocatalyst processing methodology to obtain immobilized semiconductors is by thermal spraying. There are few studies on perovskite coatings by thermal spray (TS) process for photocatalytic applications. Most of them are related to  $\text{TiO}_2$  coatings deposited by TS processes, including atmospheric plasma spraying (APS), suspension plasma spraying (SPS), flame spraying (FS), high-velocity oxy-fuel (HVOF) spray, and cold-spray for photocatalytic applications (Ref 22–24). Some reports of NBT (Ref 25) and KNN (Ref 26) coatings deposited by APS mainly discuss their ferroelectric and piezoelectric performance.

The processing of functional ceramic coatings by TS poses significant challenges to keep their performance comparable to that of bulk sintered ceramics. However, TS techniques rely heavily on the optimization of processing parameters to achieve the desired results. In particular, perovskite-type functional coatings deposited by TS can undergo significant physical and chemical transformations during particles in-flight through the plasma (PS) (Ref 27). Preferably, the goal in the literature has been to achieve single-phase, fully crystalline, dense, or defect-free coatings, which is not a simple task for perovskite-type materials. However, several processing difficulties are encountered in practice. For instance, it has been reported that in the case of NBT or KNN-based materials deposited by PS, severe loss of  $\text{Bi}_2\text{O}_3$  or  $\text{Na}_2\text{O}$  occurs, which can be

solved by excess addition of these volatile oxides (up to 10 mol.%) to maintain the perovskite stoichiometry (Ref 28, 29) Another problem is associated with the high cooling rates in PS that prevent complete recrystallization. On the other hand, it has been reported that fuel-rich combustion conditions lead to oxygen vacancy formation due to  $Ti^{3+}$  defects, which affect the dielectric properties (Ref 30). However, the reactions that take place during the TS process are not always negative, especially when pursuing applications where multiple interlayers are required, for instance, between two or more semiconductors for photocatalytic applications.

FS is a versatile, cost-effective, and simple thermal-spray combustion method, in which multiple parameters can be adjusted to achieve different results. Some of its processing parameters are material type, morphology, size distribution, fuel/oxygen (F/O) ratio, gas flow rate (TF), stand-off distance (SOD), etc. (Ref 31). FS uses the chemical energy from the combustion of oxygen ( $O_2$ )-acetylene ( $C_2H_2$ ) gas to generate a hot flame in the spray torch. Particles or droplets of the fed material are accelerated toward the workpiece by the expanding hot gas flow and air jets. Adjusting the F/O ratio on either side of the stoichiometric ratio will cool the flame, producing oxidizing or reducing (fuel-rich) plume conditions, which can be selected according to the desired characteristics of the sprayed material (Ref 32). The highest combustion temperature reached at atmospheric pressure is 3410 K, and the maximum temperature that the particles can achieve ( $T_p$ ) relative to the gas temperature ( $T_g$ ) after their flight is about 0.7 to 0.8  $T_g$  (Ref 31). Flame velocities in FS are typically below 100 m/s, generating particle velocities up to 80 m/s before impact. The microstructure and properties of the sprayed coatings are highly dependent on all phenomena occurring during particle flight (Ref 33).

Recently, a novel process for obtaining in situ heterojunctions of different semiconductors by FS processing with photocatalytic applications was reported (Ref 16, 34). For instance, Bi/ $\beta$ - $Bi_2O_3$  heterojunctions in powder that are photoactive in visible-light were obtained by FS. The flame chemistry and the high temperature reached in the combustion reaction allowed efficient semiconductor coupling, leading to the formation of Janus particles (nano or microparticles whose surfaces have two or more distinct physical properties), enhancing charge carrier transfer and reaction. This work builds on the experience observed in powders with the objective of tuning the optical properties in NBT-based coatings for photocatalytic applications by in situ formation of heterostructures within the in-flight particles in the plume of the FS process.

NBT coatings deposited by FS have not yet been reported. Considering the reactivity phenomena of ceramic

compounds promoted by the high temperature and stoichiometric conditions of the FS plume, in which interfaces of a multiphase material are obtained from the heating history until reaching the formation of liquid phases and their subsequent extreme cooling processes, there is a great opportunity for the study of coatings containing a multiphase microstructure constituting bismuth-based heterojunctions with photocatalytic properties active in visible light.

For environmental remediation applications, the opportunities lie in the non-toxicity of Bi-based perovskites such as NBT and their advantageous multifunctional properties, as well as obtaining heterojunctions in the deposited coatings by low-cost techniques.

Previous work reported the deposition of NBT coatings by FS, where the effect of processing parameters such as the size of microspheres obtained by spray drying was mainly discussed. Partial phase decomposition of the perovskite in the coating was observed (Ref 16), leading to the formation of heterojunctions distributed throughout the coating that considerably improved its optical properties. In this work, the effect of the flame-spraying parameters on the structural, microstructural, and optical properties of coatings prepared from spray-dried and pre-sintered NBT microspheres is reported. In addition, the photoelectrochemical properties of NBT powder and coating samples were evaluated by cyclic voltammetry, open circuit potential, Mott–Schottky plots, and chronoamperometry.

## Experimental Procedure

### Synthesis and Processing of Feeding Powder

NBT powder was synthesized by mixing commercial oxide precursors by ball milling followed by a calcination-activated solid-state reaction. Stoichiometric amounts of  $Bi_2O_3$  (Sigma-Aldrich, 99.9%),  $Na_2CO_3$  (Meyer, 99.5%), and  $TiO_2$  (Sigma-Aldrich, 99.0%) were mixed and milled in a planetary mill (PM 400, Retsch) for 2 h at 250 RPM. Yttria-stabilized zirconia (YSZ) balls and methanol contained in an  $Al_2O_3$  jar were used as milling media. Heat treatment for solid-state reaction step (calcination) was performed twice at 920 °C for 5 h and then milled in a planetary mill for 1 h at 150 RPM. This step was performed based on our research group previous experience of in the synthesis of NBT-based materials which has shown that the calcination step performed several times improves the purity of NBT (Ref 13). Next, the NBT powder was agglomerated into particles with spherical morphology and a size distribution of  $d_{10} = 10 \mu m$ ,  $d_{50} = 32 \mu m$ , and  $d_{90} = 60 \mu m$  by spray

drying using laboratory scale equipment (DL 410, Yamato). Subsequently, a slurry was prepared with 20 vol.% NBT powder in distilled water and ammonium polymethacrylate (Darvan C-N, RT Vanderbilt, Norwalk, CT) as a binder. Spray-drying parameters were set at 1 kPa atomization pressure, 10 mL/min feed rate, 220 °C inlet temperature, 0.4 m<sup>3</sup>/min airflow rate, and a 2.55 mm nozzle (No.5) was used. The agglomerated particles were consolidated by a sintering at 1000 °C, for 2 h. Further details of the NBT powder fabrication process and its microstructural characteristics are described elsewhere (Ref 16).

### Flame Spray Coatings Process

NBT coatings were deposited by FS using an oxygen-acetylene torch (6P-II ThermoSpray™ Gun, Oerlikon Metco) with a P7C-K nozzle. The spray gun was manipulated with a 6-axis robotic arm (KRC2, Kuka). NBT microspheres were fed to the nozzle torch using a volumetric powder feeder (P-50, Flame Spray Technologies) with N<sub>2</sub> as the carrier gas. The powder was deposited on 26 × 26 × 3 mm copper substrates (Cu 101). Before the FS process, the surface of the substrates was grit-blasted with ANSI G-24 alumina at an air pressure of 100 psi, cleaned, and degreased in an ultrasonic bath with acetone and ethanol separately. The spray parameters F/O, SOD, and TF of oxygen and acetylene gases were varied to study the effect on the characteristics and properties of the coatings. The spray parameters that were kept fixed are summarized in Table 1. The two selected F/O correspond to a fuel-rich flame with a temperature of 3430 K, and an oxidizing type of flame with a lower temperature (3276 K). TF was set at 37 nlpm for the reducing flame and varied between 37 and 47 nlpm for the oxidizing. The SOD used for the three processing conditions was 10 and 15 cm, labeled as A and B, respectively (Fig. 1a).

**Table 1** Flame spray parameters that were kept constant during the deposition process of NBT coatings

Flame spray parameters	Value
Carrier gas (N <sub>2</sub> ) flow	12 nlpm
Air pressure	20 Psi
Oxygen pressure	30 Psi
Acetylene pressure	10 Psi
Powder feed rate	25 g/min
Pre-heating gun passes	2
Spraying passes	10
Raster speed	0.4 m/s

### Structure and Microstructure

The phases and crystal structure of the NBT coatings were identified by X-ray diffraction (XRD) in a Rigaku SmartLab diffractometer with a Bragg–Brentano geometry using Cu radiation ( $\lambda_{\text{Cu}} = 1.542 \text{ \AA}$ ), 40 kV, and 44 mA, a step size of 0.01° and a scan rate of 4°/min from 20 to 80° in 2-theta. The degree of crystallinity (DOC) was calculated from the total areas under the defined crystalline and amorphous components as  $\text{DOC} = A_{\text{cryst}} / (A_{\text{cryst}} + A_{\text{amorph}})$ , where  $A_{\text{cryst}}$  and  $A_{\text{amorph}}$  are the crystalline and amorphous peak areas, respectively. For this purpose, the X-ray diffraction areas of the coatings were determined by deconvoluting the peaks of the patterns with the Fityk software (Ref 35), using a Gaussian function. The identified crystal phases of the coatings and their quantification by weight percent (wt.%) were performed by Rietveld refinement using the GSAS software (Ref 36), obtaining in all cases refinement quality parameters of goodness coefficient ( $\chi^2$ ) and structural factor (R) values of < 1 and < 0.3, respectively.

X-ray photoelectron spectroscopy (XPS) was performed in an ultra-high vacuum (UHV) using a K-Alpha™ X-ray photoelectron spectrometer equipped with a monochromatic Al-K $\alpha$  source (1486.7 eV, 13 kV). The steps were 1 eV and 0.1 eV for the general and high-resolution spectra, respectively. The binding energies (BE) were measured by taking the C1s peak at 284.8 eV as a reference. The peak area was calculated after fitting the experimental spectra to a mixture of Gaussian and Lorentzian curves or Lorentzian asymmetric line shapes. Quantification of the atomic fractions at the surface of the solids was obtained by integrating the normalized peaks with atomic relative sensitivity factors (RSF).

The microstructure of the coatings and powder particles was characterized by micrographs measured with secondary electrons (SE) and backscattering (BSE) detectors using an environmental scanning electron microscope (XL30 ESEM, Philips). A chemical composition map of coating sample 1-A was measured using an energy dispersive spectroscopy analyzer (6I10 XFLASH, Bruker) coupled to the Philips XL30 microscope. The coating samples were encapsulated in acrylic resin, grinded, and polished sequentially with SiC paper of different sizes and colloidal silica in the final polishing step to reveal the microstructure of cross sections.

### Optical Properties

The optical absorption properties and bandgap of the coatings were measured by recording diffuse reflectance spectra (DRS) in the range of 200–1100 nm using an Agilent Technologies Cary Series UV–vis-NIR

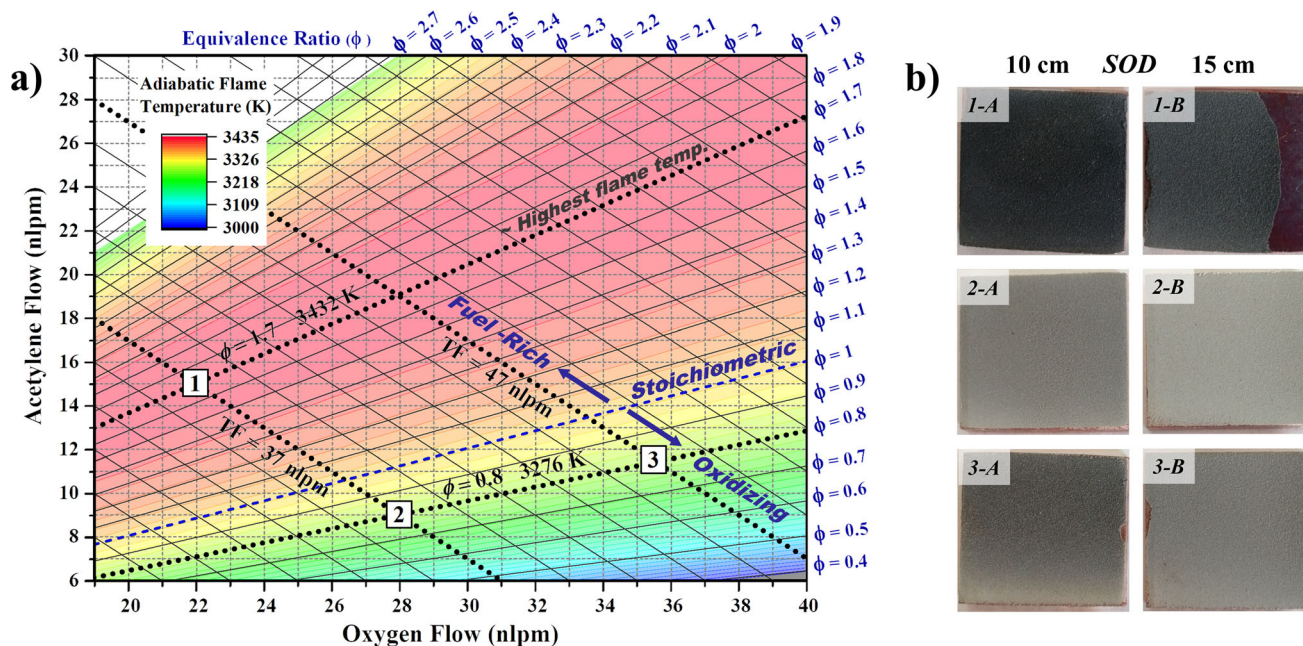


**Fig. 1** (a) Flame spray conditions (1, 2, and 3) for the processing of NBT coatings, defined by the equivalence ratio ( $\phi$ ), total gas flow (TF), and flame temperature as a function of the oxygen and acetylene

gas flow. (b) Images of the coatings deposited at a SOD of 10 and 15 cm (A and B respectively)

spectrophotometer with an integrated sphere. The measured reflectance data  $R$  were transformed to the Kubelka-Munk function  $F(R)$  (Eq 1) to determine the value of the band gap via the Tauc plot (Eq 2) by plotting  $(F(R)hv)^{1/n}$  versus  $hv$ .

$$F(R) = \frac{(1 - R)^2}{2R} \tag{Eq 1}$$

$$(F(R)hv)^{1/n} = C(hv - E_g) \tag{Eq 2}$$

where  $F(R)$  is a function of reflectance and is proportional to the extinction coefficient  $\alpha$  used for highly scattering samples.  $R$  is the reflectance measured by UV-Vis spectrophotometry,  $hv$  is the energy of the photons induced,  $n$  is the optical transition,  $C$  is a constant, and  $E_g$  is the band gap energy of the bulk of the semiconductor. The optical transition can be  $n = 1/2$  for a direct transition and  $n = 2$  for an indirect transition.

**Photoelectrochemical Measurements**

Cyclic voltammetry (CV), open circuit potential (OCP), chronoamperometry (CA), and Mott-Schottky (M-S) measurements were carried out to study the photoelectrochemical properties of the coatings.

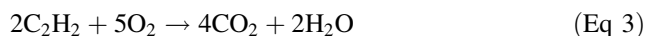
Electrochemical characterization was performed in a standard three-electrode electrochemical cell configuration, in which deposited fluoride-doped tin oxide (FTO) glasses, AgI/AgCl<sub>(sat)</sub>, and a graphite rod served as working,

reference, and counter electrodes, respectively. A 0.3 M K<sub>2</sub>SO<sub>4</sub> (pH = 7) solution was used as the supporting electrolyte. The working electrodes were prepared by using a spray pyrolysis deposition technique. For this purpose, the powder was dispersed in isopropanol, formulated with 10 gL<sup>-1</sup> and sprayed onto transparent electrically conductive FTO glasses (15 Ω-sqr), which were cleaned in an ultrasonic bath with acetone, isopropanol, and deionized water for 0.5 h before use. Two samples were prepared, the synthesized NBT powder and the NBT coating 1-A, which prior to deposition on FTO, was detached from the Cu substrate and milled in a mortar. The samples prepared on FTO were annealed at 500 °C, for 2 h in air at a rate of 5 °C/min. CA measurements were performed under UV irradiation ( $\lambda = 365$  nm, irradiance  $I_0 = 2$  mW/cm<sup>2</sup>) and visible LED light (10W, 3500 K).

**Results and Discussion**

Figure 1(a) shows the deposition conditions of the coatings (1, 2, and 3) defined by the equivalence ratio ( $\phi$ ), the adiabatic flame temperature (AFT) calculated at 1 atm and initial temperature of 298 K (Ref 37), and the TF as a function of the acetylene and oxygen gas flow. In combustion reaction processes, the flame temperature depends on the F/O ratio. For most systems, the maximum temperature is reached around the stoichiometric mixture, at which the combustion reaction is complete (Eq 3). The  $\phi$

described in Eq 4 is a normalized mixing ratio to express the deviation from the stoichiometric condition defined as the actual F/O ratio relative to the stoichiometric on a molar or mass basis, where  $F$  corresponds to fuel and  $A$  to the comburent (volume or mass). For a stoichiometric mixture  $\phi = 1$ , fuel-rich systems  $\phi > 1$  and fuel-poor systems  $\phi < 1$  (Ref 31) as shown in Fig. 1(a). The peak flame temperature of the oxy-acetylene combustion system is reached on the fuel-rich side due to the higher bond dissociation energy of CO, which manifests itself in a lower dissociation of the combustion products and the consequent higher temperature (Ref 38). The AFT is a good estimate of the maximum temperature reached during a combustion reaction and can be calculated as the energy balance of a steady-flow combustion process, assuming a chemical equilibrium of the gaseous mixture ( $\phi$ ) with no heat loss, subjected to pressure and enthalpy constraints.



$$\phi = (F/A)/(F/A)_{\text{stoichiometry}} \quad (\text{Eq 4})$$

The conditions under which the coatings were deposited on the AFT show differences in their color, as observed in the images of coatings deposited at a SOD of 10 cm (A) and 15 cm (B), respectively (Fig. 1b). For instance, coating 1-A falling on the darkest color was deposited with the highest amount of fuel ( $\phi = 1.7$ ) at the shortest distance (SOD = 10 cm) and a lower flow of gases (TF = 37 nlp/m), while coating 2-B falling on the lightest area corresponds to the sample deposited with a flame with an excess of oxygen ( $\phi = 0.8$ ) at a longer distance (SOD = 15 cm), and low total flow gases (TF = 37 nlp/m). The effect of the processing conditions is discussed below.

## Structural and Microstructural Properties

Figure 2(a) shows the XRD patterns of the as-sprayed coating samples 1-A, 1-B, 2-A, 2-B, 3-A, 3-B, and the NBT powder fed to the flame gun for comparative purposes. Peak positions and relative intensities of the NBT lattice plane reflections corresponding to a perovskite crystal structure of rhombohedral symmetry ( $R3c$ ), indexed with COD ID 2103295 (●), which was also identified in the feeding powder diffractogram (gray color) can be observed in the diffraction patterns of the coatings. XRD patterns of coatings 1-A, 1-B, 2-B, 3-A, and 3-B show additional low intensity diffraction peaks in the  $2\theta$  range of  $24\text{--}29^\circ$ . In the coatings deposited with spraying condition 1,  $TiO_2$  of anatase and rutile phases were identified and indexed with COD ID 9008215 (A) and 9004142 (R), respectively. In addition, in these coating samples and samples 2-B, 3-A, and 3-B, a low intensity peak centered at  $30.1^\circ$  corresponding to the Aurivillius  $Bi_4Ti_3O_{12}$  (B) phase, indexed with COD ID 1528445 was identified. The diffraction patterns of the coatings also show a distinct broad diffuse background at  $2\theta$  25 to  $35^\circ$  corresponding to a non-crystalline phase. This feature has been observed previously in NBT flame-sprayed coatings (Ref 16) and in other perovskite ceramic coatings thermally sprayed in the as-sprayed condition (Ref 39–41). During the thermal-spray process, after the particles reach a molten state due to their exposure to the flame temperature and subsequently impact against the substrate, accelerated heat transfer phenomena will occur with high cooling rates, which prevents the formation of a long-range ordered phase. Figure 2(b) shows the Rietveld refinement analysis of the as-sprayed sample 1-A, where a combination of amorphous and crystalline

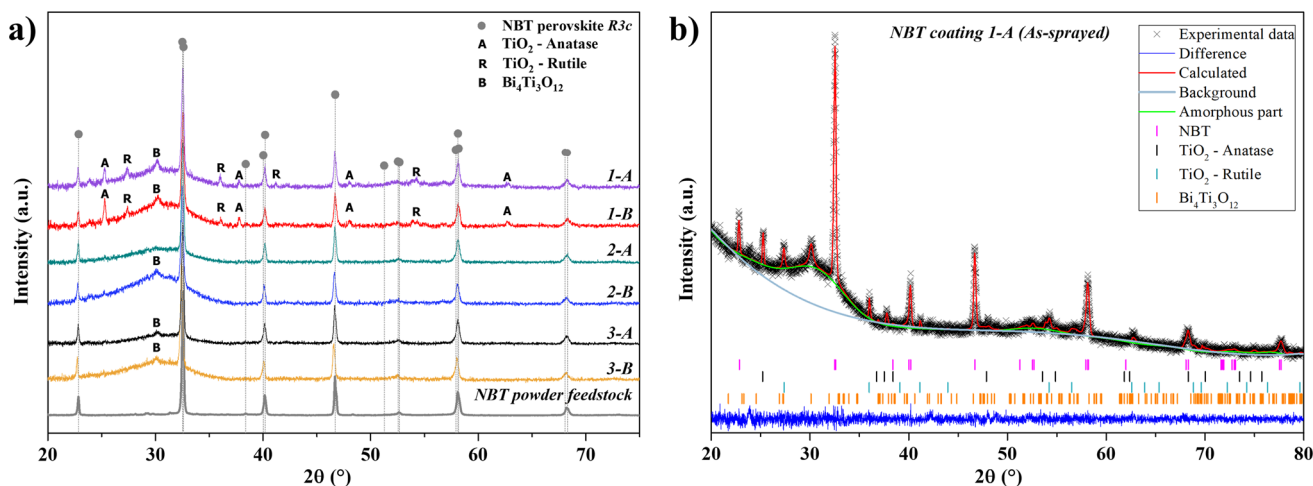


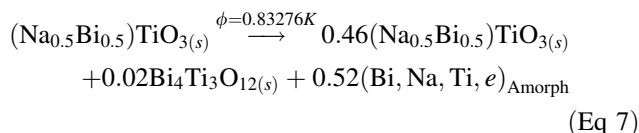
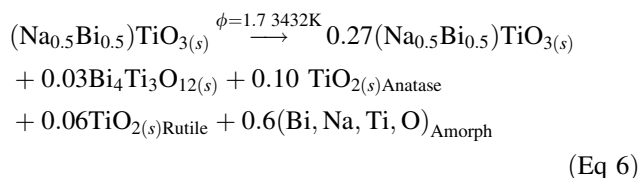
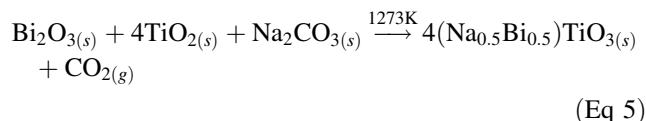
**Fig. 2** (a) XRD patterns of the as-sprayed NBT coatings and the powder fed to the flame gun, (b) Rietveld refinement analysis of the diffractogram of 1-A NBT coating sample

phases is observed. The information from the structural analysis, DOC, and phase weight fractions of the coatings are summarized in Table 2. According to the results, the DOC is higher at spray distances of 10 cm (39.6–48.5%) than at 15 cm (24.3–35.1%).

The crystalline phases of the coatings, NBT perovskite, TiO<sub>2</sub>-Anatase, TiO<sub>2</sub>-Rutile, and Bi<sub>4</sub>Ti<sub>3</sub>O<sub>12</sub> were identified and quantified in weight percent (wt.%) by Rietveld refinement. The predominant crystalline phase (free of amorphous phases) in all coatings is NBT perovskite, with sample 2-A having the highest content (100 wt.%). The crystalline fraction of Bi<sub>3</sub>Ti<sub>4</sub>O<sub>12</sub> content was less than 10.6 wt.% in all coatings. The presence of TiO<sub>2</sub> phases only in coating samples 1-A and 1-B (up to 19.2 wt.% as anatase and 14.2 wt.% as rutile) is attributed to the higher heat input and a reducing flame atmosphere provided by  $\phi = 1.7$ . A significant effect of the thermal spray process on the structural properties of NBT is evident. The reactions started with the melting of the in-flight NBT particles occurring at  $\sim 1225$  °C, which is the temperature of NBT (congruent) melting (Ref 42). Since the flame temperatures produced are  $> 2000$  °C, a melting state of the particles can be reached. It has been reported that processing of NBT ceramic at high temperatures result in loss of Bi<sub>2</sub>O<sub>3</sub>/Na<sub>2</sub>O starting at  $\sim 1150$  °C with significant volatilization of Bi<sub>2</sub>O<sub>3</sub> (Ref 42). Subsequent cooling of the Bi-deficient melt resulted in recrystallization of NBT, TiO<sub>2</sub>, and Bi<sub>4</sub>Ti<sub>3</sub>O<sub>12</sub>, and a remanent amorphous phase was formed by rapid cooling (Eq 6 and 7).

The initial formation of the metastable TiO<sub>2</sub> anatase phase and further transformation to the rutile phase require sufficient thermal energy to facilitate the rearrangement of the atoms. This transition occurs above 600–700 K, and it has been reported that heating under low oxygen partial pressure conditions in a reducing or neutral atmosphere enhances the transformation by increasing the density of oxygen vacancies (Ref 43).

Solid-state reaction



As mentioned before, the chemical composition and elemental oxidation state of the elements present in the NBT, and the coatings obtained at 10 cm (1-A, 2-A, and 3-A) were investigated by XPS. Table 3 shows the quantification according to the XPS survey scan spectrum, revealing that the NBT sample includes Bi (42.1 wt.%), Ti (13.9 wt.%), O (26.2 wt.%), Na (8.0 wt.%), and adventitious C (9.8 wt.%). After the coating process, the chemisorbed C increases to 64.1, 71.1, and 49.4 wt.% for 1-A, 2-A, and 3-A, respectively. On the other hand, the amount of Ti with respect to Bi (Bi wt.%/Ti wt.%) increases from 3.0 in NBT to 10.3 for 2-A, which shows that the surface of the coatings is richer in Bi compared to NBT. This is because the Bi volatilizes and subsequently recrystallizes on the coating surface. The high Bi/Ti ratio on the surface can be correlated with a lighter color of the material, as shown in Fig. 1(b) for samples 2-A and 2-B. The surface of the coating also shows the presence of traces of N 1s, less than 1.0 wt.%, which are likely formed by the N<sub>2</sub>-rich atmosphere used as a carrier gas to feed the NBT powder.

**Table 2** Summary of processing parameters and properties of NBT coatings

Sample	F/O ( $\phi$ )	TF, nlpm	SOD, cm	Thickness, $\mu\text{m}$	E <sub>g</sub> , eV	DOC, %	Crystalline phase fraction, wt.%			
							NBT	TiO <sub>2</sub> (Anatase)	TiO <sub>2</sub> (Rutile)	BTO
1-A	1.7	37	10	162.0 ± 17.2	2.63	39.6	67.6	9.9	14.2	8.5
1-B	1.7	37	15	152.4 ± 12.0	2.81	32.0	61.4	19.2	8.8	10.6
2-A	0.8	37	10	117.0 ± 17.5	2.96	40.4	100	...	...	...
2-B	0.8	37	15	69.6 ± 8.10	2.95	24.3	90.2	...	...	9.8
3-A	0.8	47	10	173.8 ± 26.5	2.90	48.5	95.1	...	...	4.9
3-B	0.8	47	15	113.6 ± 10.4	2.93	35.1	94.9	...	...	5.1

Microstructural, structural, and optical properties.

**Table 3** Quantification of the different elements according to the XPS survey spectra for powder feedstock (NBT) and the coatings deposited at a SOD of 10 cm (1-A, 2-A, 3-A)

Sample	Element, wt.%						Bi/Ti, wt.%/wt.%
	C	O	Na	Ti	Bi	N	
BNT	9.8	26.2	8.0	13.9	42.1	0.0	3.0
1-A	64.1	18.8	4.2	1.9	10.0	1.0	5.2
2-A	71.1	16.7	5.9	0.5	5.1	0.7	10.3
3-A	49.4	19.9	4.6	3.1	22.2	0.8	7.2

Figure 3(a), (b), and (c) show the high-resolution XPS spectra of Bi 4*f*, Ti 2*p*, and O 1*s*, respectively. Complementarily, Table 4 shows the assignments of the main spectral bands based on their binding energies (BE) and weight percent (wt.%). The Bi 4*f* spectrum for NBT shows two sharp peaks at 159.0 and 164.3 eV, corresponding to the binding energies of Bi 4*f*<sub>7/2</sub> and Bi 4*f*<sub>5/2</sub>, respectively. The high-resolution XPS spectra for the coating (1-A, 2-A, and 3-A) show changes mainly in Bi 4*f* and O 1*s*. The signal for Bi 4*f* can deconvolute into two doublets; the new signal for Bi 4*f*<sub>7/2</sub> is present around 159.0–159.1 eV and can be assigned

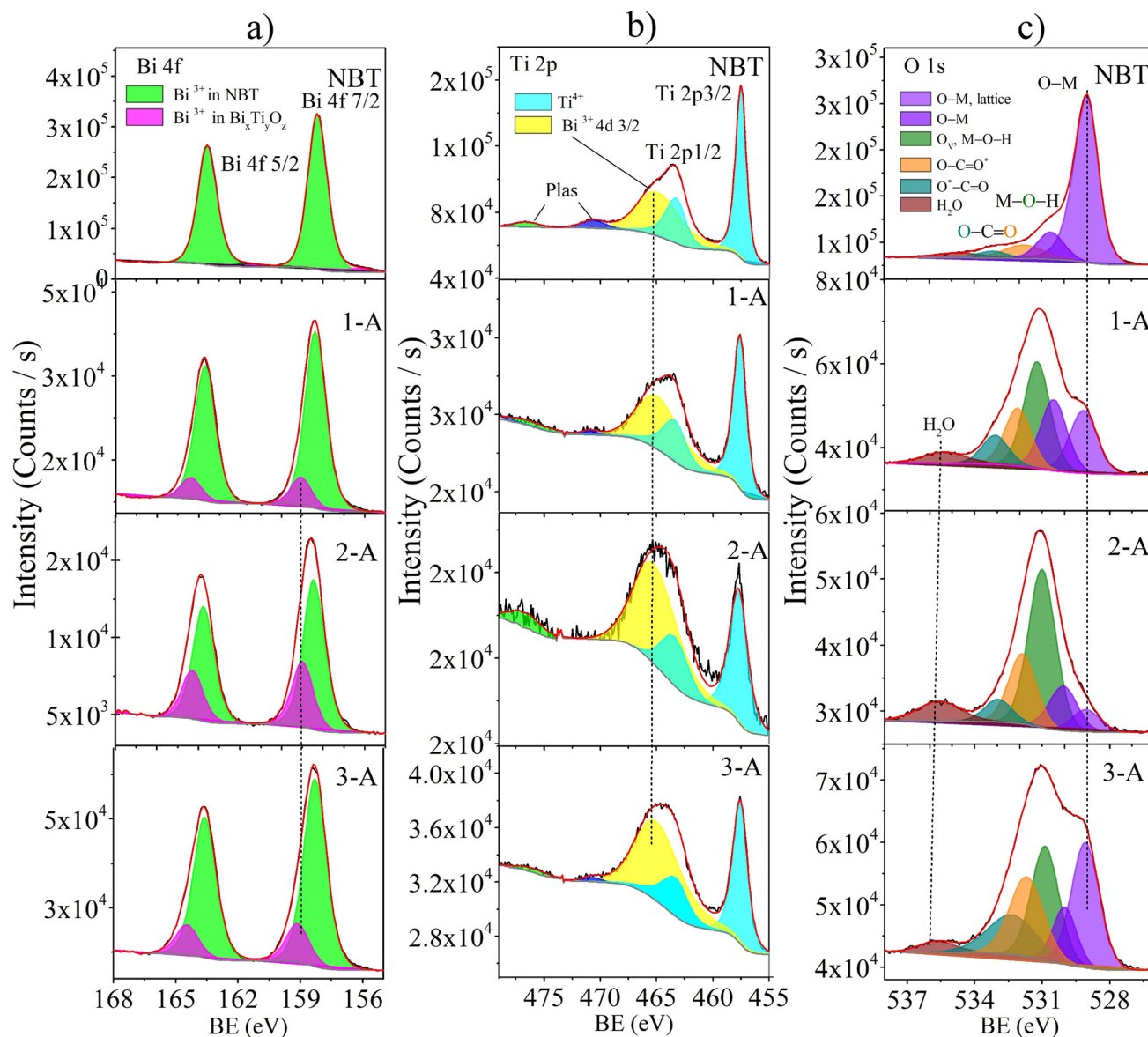


**Fig. 3** High-resolution XPS spectra for Bi 4*f*, Ti 2*p*, and O 1*s* for the powder feedstock (NBT) shown at the top, and the coatings deposited at a SOD of 10 cm (1-A, 2-A, and 3-A)



**Table 4** Assignments of main spectral bands based on their binding energies (BE) and weight percentage (wt.%) for powder feedstock (NBT) and the coatings deposited at a SOD of 10 cm (1-A, 2-A, 3-A)

Element	Assignments	Sample							
		NBT		1-A		2-A		3-A	
		BE, eV	wt.%	BE, eV	wt.%	BE, eV	wt.%	BE, eV	wt.%
Bi $4f_{7/2}$	Bi <sup>3+</sup> in NBT	158.3	100.0	158.4	86.7	158.5	70.3	158.4	82.5
	Bi <sup>3+</sup> in BTO	0.0	0.0	159.1	13.3	159.0	29.7	159.1	17.5
Ti $2p_{3/2}$	Ti <sup>4+</sup>	457.5	100	457.6	100.0	457.7	100	457.6	100.0
O 1s	O-M, Lattice	529	72.1	529.2	18.6	529.0	6.4	529.1	26.8
	O-M	530.6	12.1	530.5	20.0	530.1	12.8	530.0	10.2
	O <sub>v</sub> , M-O-H	531.8	8.9	531.2	31.0	531.0	45.5	530.9	24.2
	O-C=O*	0.0	0.0	532.1	16.8	531.9	20.2	531.7	20.9
	O*-C=O, O-C-O	533.2	3.1	533.1	8.4	532.9	6.4	532.3	14.8
	H <sub>2</sub> O	534.7	3.7	535.3	535.3	535.6	8.7	535.6	3.1
	Na 1s	Na <sup>+</sup>	1070.8	100.0	1070.9	100.0	1071.0	100.0	1071.0

either to Bi<sub>4</sub>Ti<sub>3</sub>O<sub>12</sub> (Ref 44) or bismuth oxides (Ref 45). In the Ti 2p spectrum, a broad peak is observed around 465 eV, which is due to the partial overlap of Ti 2p<sub>1/2</sub> and Bi 4d<sub>3/2</sub>. According to the peak deconvolution, the binding energies for Ti 2p<sub>3/2</sub> and Ti 2p<sub>1/2</sub> are observed at 457.5 and 463.3 eV, respectively, implying the existence of a Ti<sup>4+</sup> oxidation state. The XPS spectra for O 1s show the signal corresponding to oxygen in the lattice (529.0-529.2 eV, M-O). Other signals at 530.0-530.6 eV may correspond to the presence of other oxides, such as those present in amorphous phases (see Eq 6 and 7). Moreover, the signal (531.7-532.1 eV) can be assigned to oxygen vacancies (O<sub>v</sub>) (Ref 46). However, there has been a recent discussion about the wrong assignment of this signal, which can be due to the adventitious hydroxyls of water adsorbed on the oxides under ambient conditions forming (M-O-H) (Ref 47). The signal at higher binding energy corresponds to the chemisorbed oxygen in the single and double bonds of the O-C=O specie (indicated by an asterisk) at 531.7-532.1 eV (O-C=O\*) and 532.3-533.2 eV (O\*-C=O), whereas the signal for chemisorbed H<sub>2</sub>O is found at values of 534.7-535.6 eV (Ref 47). The results show that a higher number of O<sub>v</sub> or M-O-H is related to a higher amount of chemisorbed C, as well as to a higher amount of Bi<sup>3+</sup> on the surface. Finally, the position of Na 1s does not change significantly.

To estimate the efficiency of the deposition process, the thickness of the coatings was measured by analyzing at least 10 optical microscope cross sectional images of each sample. Varying the spray parameters produced different average thicknesses (Table 2), ranging from 70 to 174 μm. Figure 4 shows backscattered cross sectional micrographs corresponding to as-sprayed NBT coatings deposited at 10 cm: 1-A (a, d), 2-A (b, e), and 3-A (c, f). Some of the features observed in the coatings are a typical laminar microstructure produced by the building-up of splats (Fig. 4d). Circular solid structures (Fig. 4d) and some

cracks are also observed. Globular-like porosity and semi-molten particles are mostly observed in sample 3-A (Fig. 4f). The microstructural heterogeneities probably originate from differences in the melting state of particles reached during the FS process, which is highly dependent on their in-flight particle distribution. Micrographs of NBT in-flight particles sprayed with condition 1 and collected in water (Fig. 5c) show coarse unmelted particles with the fine-grained microstructure of the fed powder (Fig. 5b) and fully melted finer particles with a smooth surface. Depending on the microstructural features observed in the cross section of the coatings, the former type of particles may be trapped in the microstructure, bounced off, or fail to reach the substrate, and the latter forms splats or due to re-solidification their spherical shape is retained within the laminar structure.

Samples deposited with φ = 1.7 show splats of darker gray tones, indicating variations in chemical composition. On the other hand, samples deposited with φ = 0.8 show no significant shade contrasts, which may be related to temperature and oxidizing or reducing atmospheres provided by the F/O ratio. Chemical composition mapping of the cross section sample 1-A (Fig. 6a) shows that the tonality contrasts in the splats are mainly associated with differences in Bi and Ti content. The lighter regions show a composition richer in Bi and Na (Fig. 6c, d), while the darker gray ones are Bi-deficient and Ti-rich (Fig. 6b).

### Optical Properties of NBT Coatings

Figure 7(a) shows the absorbance spectra of NBT powder and coatings obtained from the measured diffuse reflectance spectra. The spectrum of the NBT powder (gray color) shows a steep absorbance edge in the UV region up to 410 nm. In the case of NBT as-sprayed coatings, the absorbance edge shifts to the visible-light region,

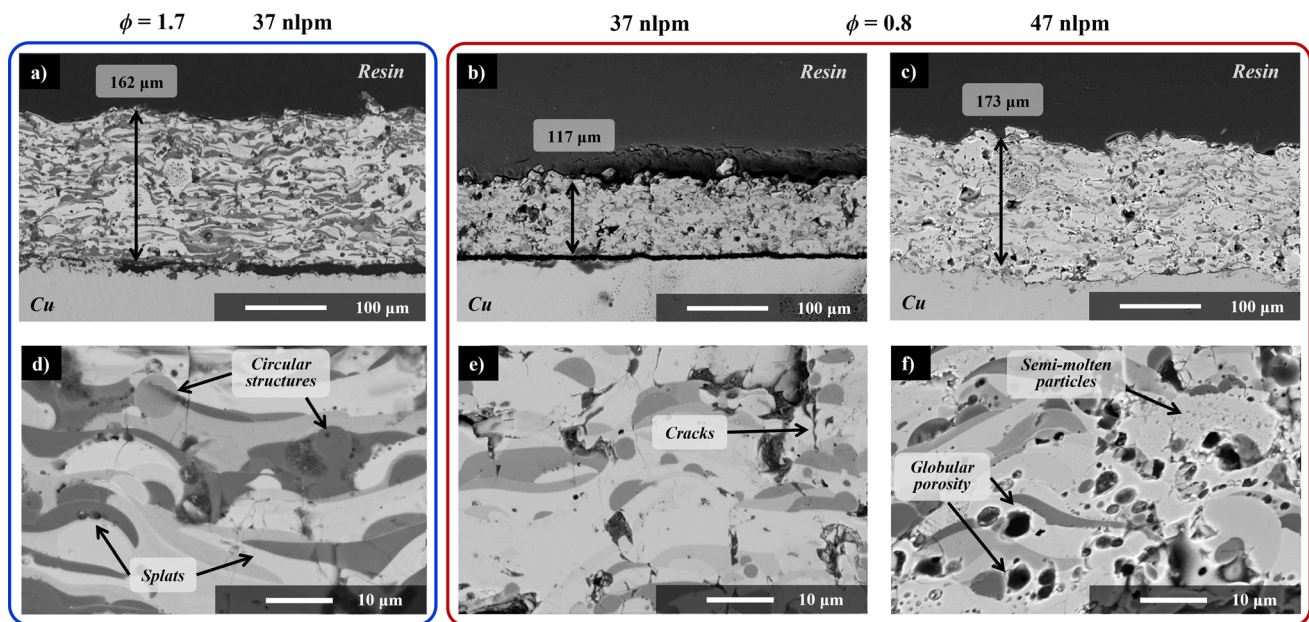


**Fig. 4** Cross sectional micrographs of the NBT coatings deposited with spraying conditions 1 (a), (d), 2 (b), (d), and 3 (c), (f) at a SOD of 10 cm

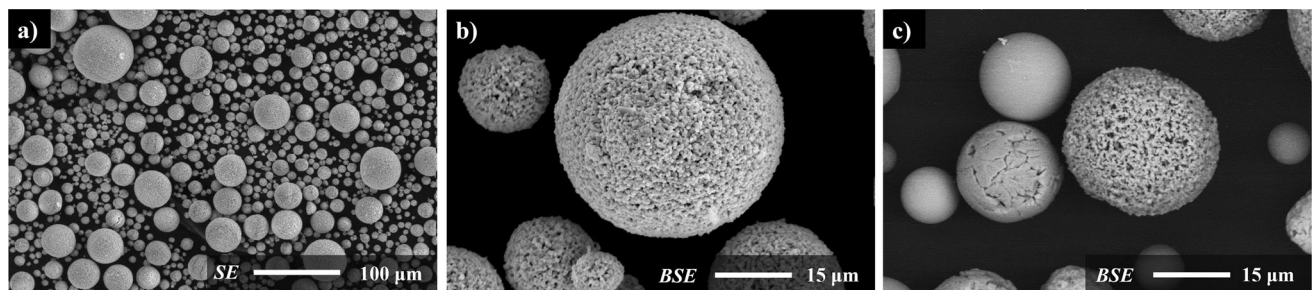


**Fig. 5** SEM micrographs of NBT fed powder particles. (a) As-spray-dried, (b) Spray-dried and sintered, and (c) Water-quenched after the flame spraying process

indicating a reduction of the band gap ( $E_g$ ). The observed differences in the light absorption properties of the coatings compared with pure NBT powder suggest an effect of FS processing on the structural properties. The light absorption capacity in the visible region of the coatings is shown in the Tauc plot (Fig. 7b) obtained from the K-M theory. A direct electronic transition  $n = 1/2$  was used for the bandgap calculations, since theoretical studies on the NBT band structure, as well as electronic and optic properties show a direct band gap (Ref 48).

The optical band gap energy values were estimated using the Tauc method by a linear fit and extrapolating the slope to  $(F(R)hv)^{1/n} = 0$ , where the x value corresponds to  $E_g$  as shown in Fig. 7(b) and the resulting values are summarized in Table 2. In general, it is observed that coating 1-A shows the highest absorption light capacity. Although the coatings are multiphase after the FS processing resulting in the assembled heterojunction and considering that the Kubelka-Munk theory can only be

applied to measure the band gap energies for homogenous catalysts, this analysis provides intuitive insight into the photoactivity of the coatings. The synthesized NBT powder has an  $E_g$  of 3.3 eV, indicating that NBT synthesized by mixed oxide and solid-state reaction is a catalyst that can only be activated under UV light. The effect of flame processing NBT to obtain all coatings is considered as a top-down approach in which a partial dissociation of NBT into different phases takes place, depending on the spray parameters. These features cause an  $E_g$  shift toward lower energies (2.63 – 2.96 eV), which in turn implies a potential red shift in the visible range. The narrow band gap energies of the NBT coatings can be attributed to observed differences in the crystal structure such as the secondary phases  $\text{Bi}_4\text{Ti}_3\text{O}_{12}$ ,  $\text{TiO}_2$  (rutile and anatase), and lattice structure defects, such as  $\text{O}_v$  produced due to the high temperature of the thermal spray process. For instance, coating 1-A presents the narrowest  $E_g$ , with a value of 2.63 eV. These microstructures allow the transfer and

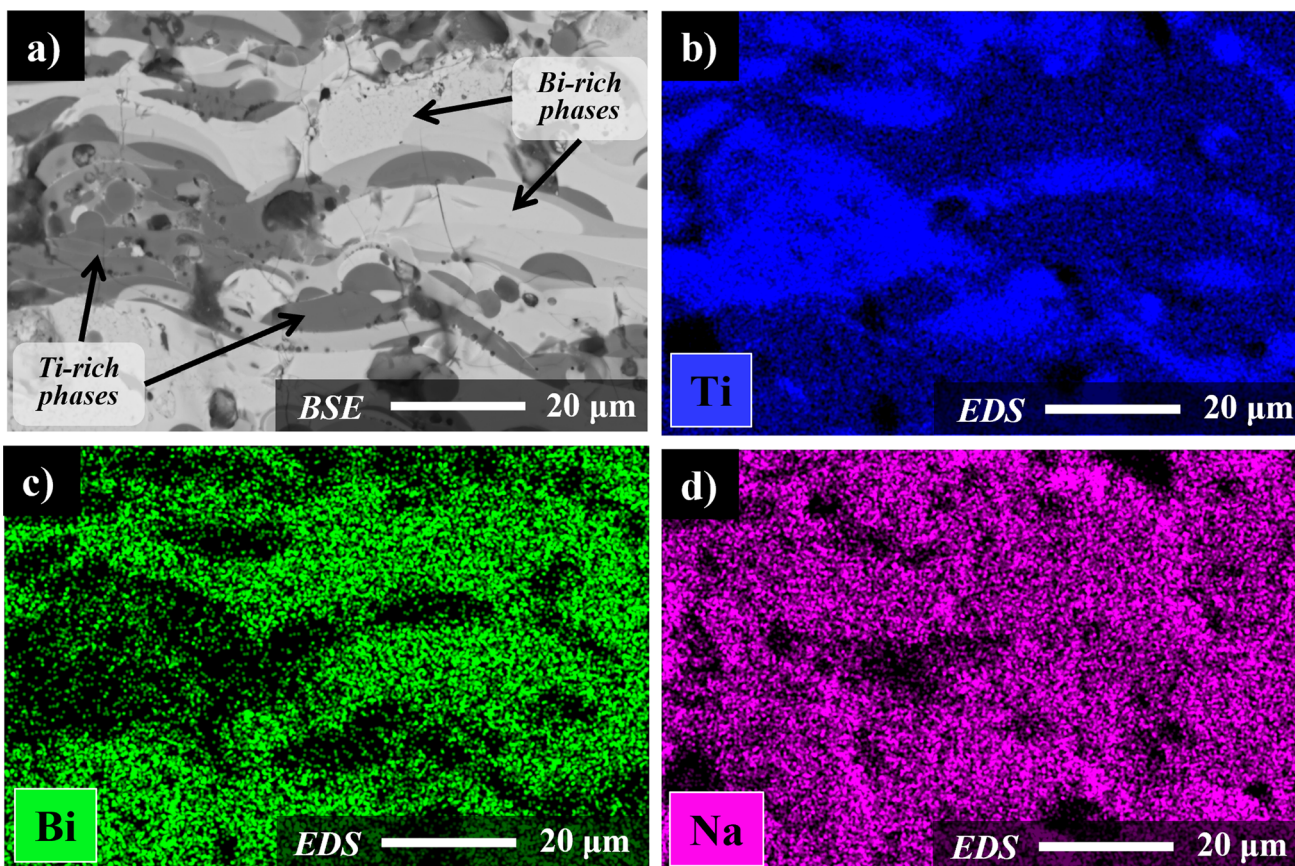


Fig. 6 EDS elemental mapping of the 1-A coating (cross section)

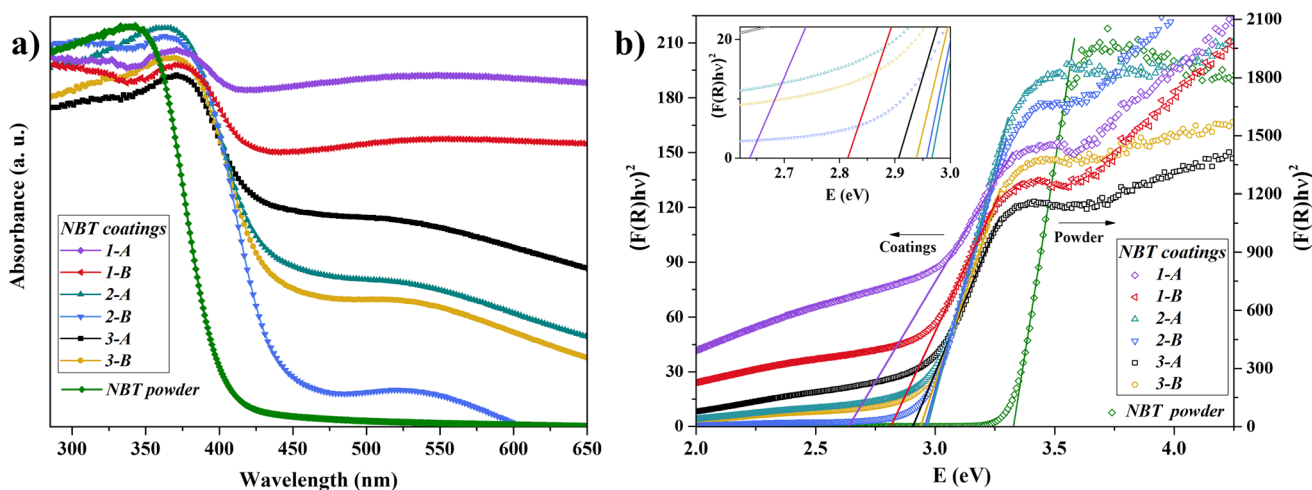


Fig. 7 (a) Absorbance spectra and (b) Tauc plot of the NBT synthesized powder and flame-sprayed coatings

migration of charge carriers between the different catalysts so that these novel heterojunctions can absorb light at lower energies.

The differences in the color shades of the coatings are consistent with the observed changes in their optical properties. In general, shade changes from light to dark

gray resulted in broader optical absorption in the visible light region and lower  $E_g$  values. Similar color variations to darker shades have been reported for reduced or partially reduced  $TiO_2$  and  $BaTiO_3$  coatings deposited by thermal spray in reducing atmosphere or low oxygen conditions (Ref 30, 49).

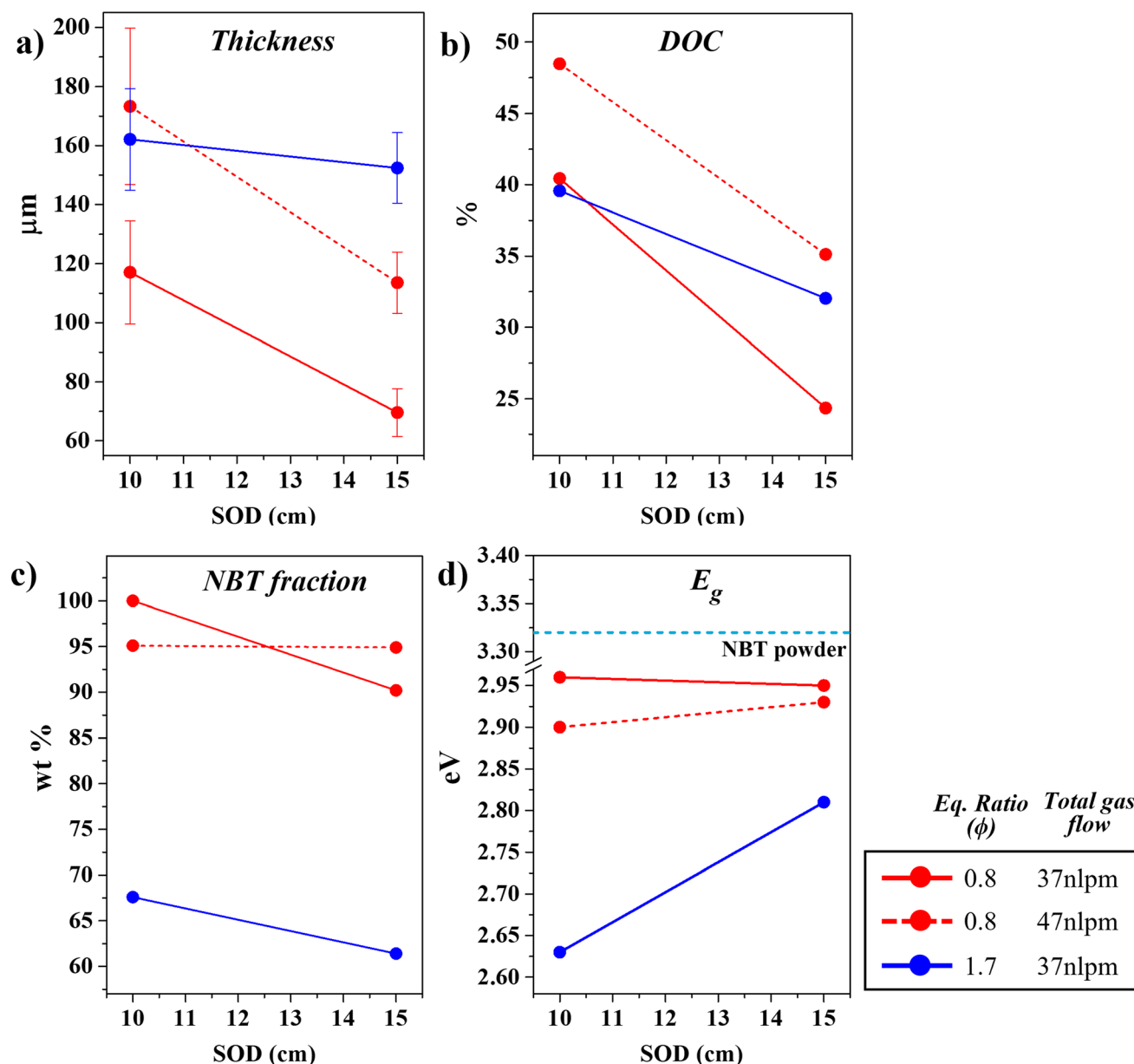


Fig. 8 Effects of the processing parameters on the NBT coatings properties as a function of the SOD, F/O, and TF

### Effect of FS Deposition Parameters on the NBT Coatings Properties

Figure 8 shows the results of the analysis of coatings properties, thickness, DOC, NBT phase content, and optical bandwidth as a function of F/O, SOD, and TF. According to the results, the coating is thicker at lower SOD in all cases, where conditions with  $\phi = 0.8$  have a more significant effect. This can be attributed to the fact that the greater the distance fewer particles reach the substrate to build up the coating. The contribution of the TF is also observed, since the higher the TF, the thicker the coating. The kinetic and thermal input provided by a higher

TF or a hotter flame ( $\phi = 1.7$ ) also promotes the increment of melting particles and their velocity which causes more particles to be deposited on the substrate. The DOC of the coatings changes as a function of the SOD and TF, being in all cases higher at a SOD of 10 cm and for  $\phi = 0.8$  at 47 nlpm. These parameters provide a higher thermal input to the substrate, producing an annealing effect on the coating layers through each pass of the torch, which reduces the cooling rate and enhances the recrystallization process.

The crystalline fraction of NBT was affected by the F/O composition, where the NBT content of coatings deposited at  $\phi = 1.7$  decreases significantly due to the formation of secondary phases. No significant effect of the SOD or FT

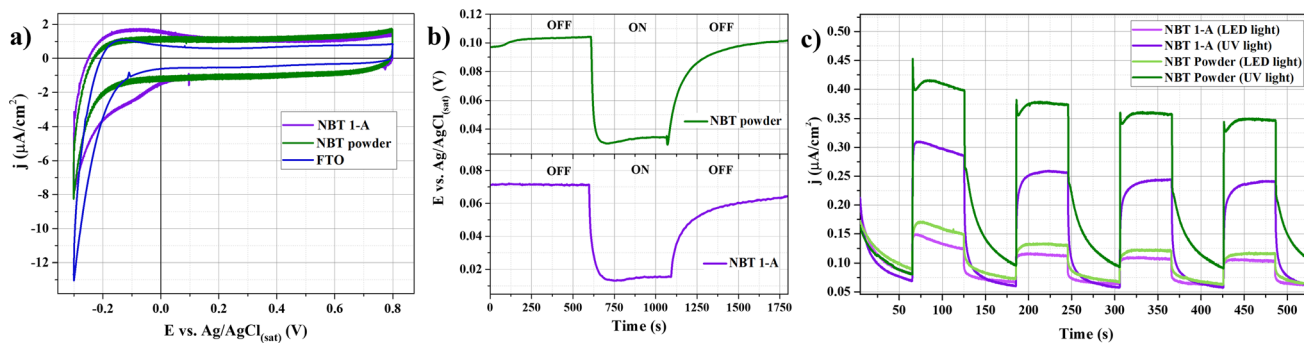


**Fig. 9** (a) Cyclic voltammograms, (b) Open circuit potentials, and (c) Chronoamperograms at open circuit potentials to measure the photovoltage generated, of NBT electrodes for precursor powder and

flame-sprayed coating 1-A at 0.8 V vs. Ag|AgCl, with a supporting electrolyte of 0.3 M  $K_2SO_4$

on the NBT content was observed. This suggests that the NBT phase transformation is mainly affected by temperature and flame chemistry. Similarly,  $E_g$  was observed to be mainly influenced by the F/O ratio, with higher  $\phi$ , narrow  $E_g$  values were obtained. In addition, a significant effect of SOD is observed at  $\phi = 1.7$ , where the shortest distance coating showed the lowest  $E_g$ .

### Photoelectrochemical Activity of NBT Powder and Coatings

Photoelectrochemical (PEC) measurements were performed to understand the mobility, transfer, and recombination of charge carriers in photoelectrodes of the as-synthesized samples in a PEC cell to determine the photocurrent density ( $j_{ph}$ ), photovoltage generated under light irradiation ( $E_{ph}$ ), and the flat band potential ( $E_{fb}$ ) of semiconductors of the NBT samples.

Cyclic voltammograms (CVs) are used to evaluate stability and quality of a photoelectrode. Figure 9(a) shows the CVs of the NBT electrode for the precursor and flame-sprayed coating samples. FTO substrate results are shown (blue line) for comparison. In general, good ohmic contact between FTO and the materials is observed, as the electrode capacitance in the anodic range ( $E > 0.2$  V versus Ag|AgCl) is higher than that of the substrate, asymptotic behavior is obtained at the zero-current line, and no faradaic signals are present. The accumulation regime for a typical n-type semiconductor is present for both materials deposited at the cathodic end of the CVs sweep. For NBT coating sample, a broad potential shoulder develops with partially reversible behavior at  $E < 0.2$  V versus Ag|AgCl. This feature, in  $TiO_2$ -based materials has been previously associated with the occurrence of charge carrier reactions, such as surface states, crystalline defects, or dopants (Ref 50). The irreversibility of the features suggests that the cathodic processes dominate over their anodic counterparts. The extent of the feature supports the idea that

charge accumulation takes place in this potential range. The absence of this feature in the NBT powder sample can be explained in terms of the microstructural properties, as pointed out in section “[Structural and Microstructural Properties](#)”, due to a higher DOC, and consequently, better electrical properties. The capacitive current observed in the most anodic region in the voltammograms indicates the potential range in which the space charge region can be studied in subsequent analyses (i.e., Mott–Schottky plots).

OCP measurements are carried out to observe the stability of the electrode without applying any potential or current perturbation under darkness or light irradiation. The first evidence of the photocatalytic activity of the catalysts under light irradiation is observed in the OCP curves. Figure 9(b) presents the photovoltage developed under UV light irradiation (ON) after an initial period in darkness (OFF). During these measurements, several photophysical processes occur concomitantly, such as exciton (electron-hole) generation, recombination, electron scavenging, etc. Therefore, both conditions (ON and OFF) are held for 600 s to achieve steady-state values since no external potential bias is applied to the materials. The NBT 1-A coating has a higher stability than the NBT powder, revealed from the initial OFF period. The measured magnitude for  $E_{ph}$  is 0.07 and 0.06 V for NBT powder and NBT 1-A samples, respectively. The ON stabilization time is similar for both materials. Faster stabilization in the OFF-recovery period is observed for the NBT powder sample, possibly attributed to faster electron transfer within the material layer, which is supported by the higher DOC.

CA measurements are conducted to examine the stability of the photoelectrode. This test provides information on the change in photocurrent density ( $j_{ph}$ ) with the time and the charge transport ability before recombination. Figure 9(c) shows the generated  $j_{ph}$  versus time curves (chronoamperograms) at a fixed potential for the samples. All samples show a fast response to the ON cycling, which supports previous observations of favorable ohmic contact.

However, a clear distinction is observed between the powder and 1-A samples during the  $j_{ph}$  relaxation, which is slower in the powder sample and with visible LED light. The  $j_{ph}$  relaxation is associated with electron migration after the abrupt interruption of irradiation, leading to the electron percolation phenomenon (Ref 51). The decay rate was fitted to the exponential function,  $J(t) = Ae^{-t/\tau_c}$ , reported by Lagemaat et al. (Ref 52), where  $\tau_c$  is the time constant for electron collection, and  $A$  is a constant. The equation considers the charge transfer mechanisms of electron collection in the range of milliseconds and longer times. Although several decay mechanisms take place during this time, such as hole recombination and scavenging from acceptor molecules in the electrolyte, it was assumed that the main mechanism must be electron collection through the film until reaching the back collector (FTO), since the potential bias is applied during the whole experiment. The  $\tau_c$  calculated for the powder sample (UV = 18.6 s, VIS LED = 21.5 s) turned out to be 62% slower than those obtained for the sample 1-A (UV = 11.5 s, VIS LED = 13.2 s). Conversely, the magnitude of the generated  $j_{ph}$  is 45 and 14% higher for the powder with UV and VIS LED light, respectively. These opposite behaviors suggest that although the powdered material can separate a higher density of electron-hole pairs, it presents less favorable electron conductivity. It is also possible to attribute the higher  $j_{ph}$  to the higher DOC of the powder sample. However, the faster electron collection is favored in the sample 1-A, possibly due to the complex interface system created by the FS.

M-S was employed for the determination of the flat band potential ( $E_{FB}$ ), one of the key factors in the analysis of the photoelectrochemical characteristics of a semiconductor that provides information on the electronic band structure of the photoelectrode and consequently its photoactivity. M-S measurements were performed for the NBT material in powder form and after the flame spray (1-A) process, which are shown in Fig. 10(a), and (b), respectively. For these measurements, a frequency sweep was performed from 100 kHz to 100 mHz, measuring 6 points per decade,

averaging the response from three measurements with a perturbation amplitude of 10 mVrms. A validity analysis was performed in terms of capacitive behavior, which is characterized by the criterion  $\partial \log Z'' / \partial \log f = -1$  (Ref 53). In our measurements, the criterion was fulfilled at frequencies between 10 and 200 Hz found in the Bode-modulus plot, with slopes of  $-0.93$  and  $-0.95$  for the powder and the 1-A samples, respectively. Linearity was evaluated by measuring total harmonic distortion (TDH < 5%) and stability was evaluated using non-stationary distortion (NSD < 3%). Figure 9(a), and (b) show the M-S curves where a positive slope is found for both samples, confirming n-type semiconductivity. The flat band potential,  $E_{FB}$  can be determined using Eq 8.

$$\frac{1}{C_{SC}^2} = \frac{2}{\varepsilon \varepsilon_0 q N_D} \left( E_{appl} - E_{FB} - \frac{k_B T}{q} \right) \quad (\text{Eq 8})$$

Where  $\varepsilon_0$  is the vacuum permittivity,  $\varepsilon$  is the material dielectric constant,  $N_D$  is the acceptor/donor density in the material,  $E_{appl}$  is the applied potential,  $E_{FB}$  is the flat band potential,  $k_B$  is the Boltzmann constant,  $T$  is the absolute temperature, and  $q$  is the elemental charge. Typically, the  $E_{FB}$  can be determined from the interception of the curve. For undoped n-type semiconductors, the  $E_{FB}$  can be assumed to merge with the conduction band potential  $E_{CB}$  (Ref 54). Therefore, the valence band potential,  $E_{VB}$ , can be estimated by adding the band gap energy to this value. For the samples evaluated, it should be noted that a mixture of complex phases with individual properties is present. Therefore, although it is not possible to determine the  $E_{FB}$  for each phase, it is plausible to obtain a statistical average value representing the energy value where that the accumulation regime relies on, i.e., an average  $E_{FB}$ . The analysis yielded convergence for the  $E_{FB}$  determination between 11 and 171 Hz, with values of  $-1.14 \pm 0.07$  V and  $-0.59 \text{ V} \pm 0.02$  versus Ag/AgCl for the powder and 1-A samples, respectively. The difference found in these values suggests that the flame spray process influences the reducing character of the material, promoting an anodic shift in this property. A smaller dispersion is also found in

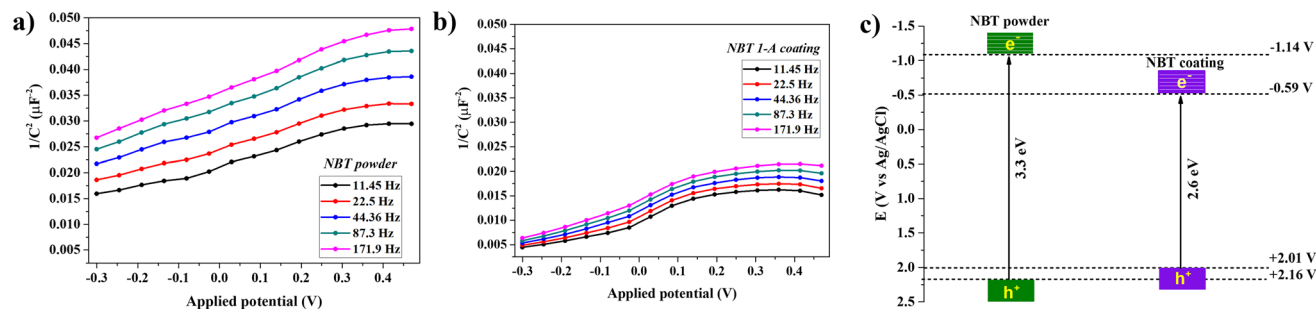


**Fig. 10** Mott–Schottky plots of NBT (a) powder and (b) 1-A coating, and (c) Schematic band edge alignment of NBT powder and 1-A coating

the 1-A sample, which can be explained in terms of the annealing of the phases during the spraying process, resulting in a smaller distribution of microstructural defects. The magnitude of the  $C_{sc}^2$  for a given frequency is smaller in the 1-A sample than that of the powder precursor, confirming a better electrical conductivity along the electrode thickness. This observation agrees with the previous findings in this section. The  $E_{CB}$  and  $E_{VB}$  band edge potentials of NBT powder and NBT coating (sample 1-A) are shown schematically in Fig. 10(c). Both materials exhibit a negative  $E_{CB}$  potential of photogenerated electrons that can scavenge molecular oxygen ( $O_2/O_2^-$ ). However, the photogenerated holes potential in VB is sufficiently positive for  $O_2/H_2O$  water oxidation. These novel semiconductors synthesized by solid-state reaction in a single-phase and processed/coupled by flame spraying to obtain multiphase conditions possess an advantageous band alignment to promote the redox reactions addressed in photocatalysis.

Considering the results presented, it can be concluded that the NBT material after FS process generates multiphase heterojunction coatings that clearly improve its photocatalytic properties, as shown by the anodic  $j_{ph}$  values. However, there seems to be a tradeoff between the DOC and the red-shifted absorbance for the sample 1-A. The tradeoff implies that a higher electron collection rate is achieved at the expense of a lower crystallinity. The latter can be explained by the coupling of the different phases and their corresponding band energy levels, as evidenced by M-S plots. Therefore, individual measurements for each phase are required to propose a mechanism to confirm this hypothesis.

## Conclusions

In the processing of photocatalytic materials under the top-down approach by flame spray processing,  $(Na_{0.5}Bi_{0.5})TiO_3$  powders lead to the decomposition of a single-phase perovskite structure to form multiphase coatings in heterojunctions. The results indicate that a flame with reducing characteristics ( $\phi = 1.7$ ) favors the formation of a combination of anatase and rutile  $TiO_2$ , and  $Bi_4Ti_3O_{12}$ , while an oxidizing flame results in a coating rich in NBT and  $Bi_4Ti_3O_{12}$ . The spray distance also plays a key role, as it influences the degree of crystallinity and the coating thickness, both parameters being higher for a shorter spray distance ( $173.8 \pm 26.5 \mu m$  and 48.5% DOC). The increase in total flow gases also generates thicker coatings. The significant structural disorder induced by the high thermal input of the flame spray process showed a large effect on the optical properties of the coating. For as-sprayed NBT coatings deposited under reducing conditions ( $\phi = 1.7$ )

photoactivity characteristics in visible light with the narrowest  $E_g$  of 2.81–2.63 eV were obtained. Moreover, PEC measurements reveal that a faster electron collection is obtained due to the flame spray process, while still retaining almost 70, and 88% of the  $j_{ph}$ , at UV and visible light, respectively. These results demonstrate the great potential of flame spray processing for the fabrication of heterostructured photocatalytic coatings, which enhances the charge transfer between the different semiconductors formed. This processing for the modification of NBT semiconductors and the coupling of the obtained phases is fast and efficient, adapting their characteristics by adjusting the flame spray processing parameters.

**Acknowledgments** The authors are grateful to CONACYT for the financial support through project 319478. This work has been carried out at CENAPROT and LIDTRA national laboratories. Special thanks to Dr. G. Torres Delgado from CINVESTAV Querétaro for the support on the measurements in the UV–vis spectrophotometer, Dr. E. F. Reguera Ruiz of the National Laboratory of Conversion and Energy Storage (LNCAE) IPN-CICATA-Legaria for the support on the XPS measurements and CIDESI for the X-ray diffraction measurements. J.A.D.-R. thanks CONACYT (“Ciencia de Frontera 2019–1” Grant Number CF-2095605) for financial support for PEC measurements equipment. C. H.-N. thanks CONACYT for the Post-doctoral Research Fellowship for the completion of this work.

## References

1. P. García-Oliveira, M. Fraga-Corral, A.G. Pereira, M.A. Prieto, and J. Simal-Gandara, Solutions for the Sustainability of the Food Production and Consumption System, *Crit. Rev. Food Sci. Nutr.*, 2022, **62**(7), p 1765–1781.
2. S. Bhandari, A. Ghosh, A. Roy, T.K. Mallick, and S. Sundaram, Compelling Temperature Behaviour of Carbon-Perovskite Solar Cell for Fenestration at Various Climates, *Chem. Eng. J. Adv.*, 2022, **10**, p 100267.
3. A.Z. Arsad, M.A. Hannan, A.Q. Al-Shetwi, M. Mansur, K.M. Muttaqi, Z.Y. Dong, and F. Blaabjerg, Hydrogen Energy Storage Integrated Hybrid Renewable Energy Systems: A Review Analysis for Future Research Directions, *Int. J. Hydrog. Energy*, 2022, **47**(39), p 17285–17312.
4. K. Li, H. Wang, J. Li, and F. Dong, Design and Mechanism of Photocatalytic Oxidation for the Removal of Air Pollutants: A Review, *Environ. Chem. Lett.*, 2022, (0123456789).
5. V. Binas, D. Venieri, D. Kotzias, and G. Kiriakidis, Modified  $TiO_2$  Based Photocatalysts for Improved Air and Health Quality, *J. Mater.*, 2017, **3**(1), p 3–16.
6. H. Yang, A Short Review Short Review on Heterojunction Photocatalysts: Carrier Transfer Behavior and Photocatalytic Mechanisms, *Mater. Res. Bull.*, 2021, **142**, p 111406.
7. A. Kumar, A. Kumar, and V. Krishnan, Perovskite Oxide Based Materials for Energy and Environment-Oriented Photocatalysis, *ACS Catal.*, 2020, **10**, p 10253–10315.
8. L. Zhang, Y. Li, Q. Li, J. Fan, A.C. Carabineiro, and K. Lv, Recent Advances on Bismuth-Based Photocatalysts: Strategies and Mechanisms, *Chem. Eng. J.*, 2020, **2021**, p 419.
9. M.K. Niranjana, T. Karthik, S. Asthana, J. Pan, and U.V. Waghmare, Theoretical and Experimental Investigation of Raman Modes, Ferroelectric and Dielectric Properties of Relaxor  $Na_{0.5}Bi_{0.5}TiO_3$ , *J. Appl. Phys.*, 2013, **113**, p 194106.

10. Y. Inoue, T. Kubokawa, and K. Sato, Photocatalytic Activity of Alkali-Metal Titanates Combined with Ru in the Decomposition of Water, *J. Phys. Chem.*, 1991, **95**, p 4059–4063.
11. I. Nomel, J. Lelievre, L. Boyer, O. Durand-Panteix, and P. Marchet, Synthesis of 0.94 Na<sub>0.5</sub>Bi<sub>0.5</sub>TiO<sub>3</sub>-0.06 BaTiO<sub>3</sub> (NBT-6BT) Lead-Free Piezoelectric Powder Suitable for Aerosol Deposition (AD), *Ceram. Int.*, 2022, **48**(10), p 14697–14707.
12. Y. Jiang, W.F. Chen, H. Ma, H. Ren, S. Lim, X. Lu, G. Bahmanrokh, S.S. Mofarah, D. Wang, P. Koshy, and C.C. Sorrell, Effect of Bi/Ti Ratio on (Na<sub>0.5</sub>Bi<sub>0.5</sub>)TiO<sub>3</sub>/Bi<sub>4</sub>Ti<sub>3</sub>O<sub>12</sub> Heterojunction Formation and Photocatalytic Performance, *J. Environ. Chem. Eng.*, 2021, **9**(6), p 106532.
13. D.A. Fernandez-benavides, A.I. Gutierrez-perez, A.M. Benitez-castro, M.T. Ayala-Ayala, B. Moreno-Murguía, and J. Muñoz-Saldaña, Comparative Study of Ferroelectric and Piezoelectric Properties of BNT-BKT-BT Ceramics near the Phase Transition Zone, *Materials (Basel)*, 2018, **11**, p 361.
14. J. Rödel, K.G. Webber, R. Dittmer, W. Jo, M. Kimura, and D. Damjanovic, Transferring Lead-Free Piezoelectric Ceramics into Application, *J. Eur. Ceram. Soc.*, 2015, **35**(6), p 1659–1681. <https://doi.org/10.1016/j.jeurceramsoc.2014.12.013>
15. M.A. Zubair, F.A. Mozahid, H. Takeda, and A.K.M.A. Hossain, Effect of Processing Temperature on Structural, Optical and Frequency Dependent Electrical Responses of Solid-State Sintered Bismuth Sodium Titanate, *Mater. Sci. Eng. B Solid State Mater. Adv. Technol.*, 2021, **274**, p 115474.
16. A.I. Gutiérrez-Pérez, M.T. Ayala-Ayala, A.G. Mora-García, B. Moreno-Murguía, H. Ruiz-Luna, and J. Muñoz-Saldaña, Visible-Light Photoactive Thermally Sprayed Coatings Deposited from Spray-Dried (Na<sub>0.5</sub>Bi<sub>0.5</sub>)TiO<sub>3</sub> Microspheres, *Surf. Coat. Technol.*, 2021, **427**(702), p 127851.
17. R. Marschall, Semiconductor Composites: Strategies for Enhancing Charge Carrier Separation to Improve Photocatalytic Activity, *Adv. Funct. Mater.*, 2014, **24**(17), p 2421–2440.
18. A. Hassani, S. Krishnan, J. Scaria, P. Eghbali, and P.V. Nidheesh, Z-Scheme Photocatalysts for Visible-Light-Driven Pollutants Degradation: A Review on Recent Advancements, *Curr. Opin. Solid State Mater. Sci.*, 2021, **25**(5), p 100941.
19. X. Xu, X. Lin, F. Yang, S. Huang, and X. Cheng, Piezo-Photocatalytic Activity of Bi<sub>0.5</sub>Na<sub>0.5</sub>TiO<sub>3</sub>@TiO<sub>2</sub> Composite Catalyst with Heterojunction for Degradation of Organic Dye Molecule, *J. Phys. Chem. C*, 2020, **124**(44), p 24126–24134.
20. D. Der Naturwissenschaften, Fabrication of Bismuth-Based Photocatalytic Heterojunctions for Hydrogen Generation Doktorin Der Naturwissenschaften María Teresa Ayala Ayala, Maestra En Ciencias, 2022.
21. M.T. Ayala Ayala, R. Dillert, J. Muñoz Saldaña, and D.W. Bahnemann, Methanol Photooxidation in a Black Body like Reactor Using Bismuth-Based Heterojunctions, *Appl. Catal. A Gen.*, 2022, **648**, p 118926.
22. M. Gardon, C. Fernández-Rodríguez, D. Garzón Sousa, J.M. Doña-Rodríguez, S. Dosta, I.G. Cano, and J.M. Guilemany, Photocatalytic Activity of Nanostructured Anatase Coatings Obtained by Cold Gas Spray, *J. Therm. Spray Technol.*, 2014, **23**, p 1135–1141.
23. H. Khatibnezhad, F. Ambriz-vargas, F. Ben Ettouil, and C. Moreau, Role of Phase Content on the Photocatalytic Performance of TiO<sub>2</sub> Coatings Deposited by Suspension Plasma Spray, *J. Eur. Ceram. Soc.*, 2022, **42**(6), p 2905–2920. <https://doi.org/10.1016/j.jeurceramsoc.2022.02.010>
24. Y. Liu, J. Huang, X. Feng, and H. Li, Thermal-Sprayed Photocatalytic Coatings for Biocidal Applications: A Review, *J. Therm. Spray Technol.*, 2021, **30**(1), p 1–24. <https://doi.org/10.1007/s11666-020-01118-2>
25. K. Guo, M.S. Misherkarloo, M. Lin, K. Yao, S. Chen, and F.E.H. Tay, Microstructure and Piezoelectric Properties of Thermal Sprayed Bi<sub>0.5</sub>(Na<sub>0.70</sub>K<sub>0.20</sub>Li<sub>0.10</sub>)<sub>0.5</sub>TiO<sub>3</sub> Ceramic Coatings, *Ceram. Int.*, 2019, **45**, p 3570–3573.
26. S. Chen, C. Kiang, I. Tan, and K. Yao, Potassium-Sodium Niobate-Based Lead-Free Piezoelectric Ceramic Coatings by Thermal Spray Process, *J. Am. Ceram. Soc.*, 2016, **7**(37661), p 1–7.
27. J. Kotlan, R.C. Seshadri, S. Sampath, and P. Ctibor, The Role of Amorphous Phase Content on the Electrical Properties of Atmospheric Plasma Sprayed (Ba, Sr)TiO<sub>3</sub> Coatings, *Ceram. Int.*, 2016, **42**, p 11010–11014.
28. K. Guo, M.S. Mirshekarloo, K. Yao, and F.E.H. Tay, Structural Evolution of Thermal Sprayed Bismuth Sodium Titanate Piezoelectric Ceramic Coatings, *J. Am. Ceram. Soc.*, 2018, **102**, p 2370–2376.
29. S. Chen, C.K.I. Tan, S.Y. Tan, S. Guo, L. Zhang, and K. Yao, Potassium Sodium Niobate (KNN)-Based Lead-Free Piezoelectric Ceramic Coatings on Steel Structure by Thermal Spray Method, *J. Am. Ceram. Soc.*, 2018, **101**(12), p 5524–5533.
30. P. Ctibor, J. Čížek, J. Sedláček, and F. Lukáč, Dielectric Properties and Vacancy-like Defects in Plasma-Sprayed Barium Titanate, *J. Am. Ceram. Soc.*, 2017, **100**(7), p 2972–2983.
31. P.L. Fauchais, J.V.R. Heberlein, and M.I. Boulos, “Thermal Spray Fundamentals; From Powder to Part, *Thermal Spray Fundam.*, 2014.
32. J.R. Davis, Associates, and ASM International. Thermal Spray Society Training Committee. Handbook of Thermal Spray Technology. ASM International, 2004.
33. L. Pawlowski, *The Science and Engineering of Thermal Spray Coatings*, John Wiley & Sons Inc, Second, 2008.
34. M.T. Ayala-Ayala, M.Y. Ferrer-Pacheco, and J. Muñoz-Saldaña, Manufacturing of Photoactive β-Bismuth Oxide by Flame Spray Oxidation, *J. Therm. Spray Technol.*, 2021, **30**(4), p 1107–1119.
35. M. Wojdyr, Fityk: A General-Purpose Peak Fitting Program, *Appl. Crystallogr.*, 2010, **43**, p 1126–1128.
36. A.C. Larson, and R.B. Von Dreele, “General Structure Analysis System (GSAS),” Los Alamos National Laboratory Report, 2004.
37. D.G. Goodwin, H.K. Moffat, I. Schoegl, R.L. Speth, and B.W. Weber, Cantera: An Object-Oriented Software Toolkit for Chemical Kinetics, Thermodynamics, and Transport Processes, 2022. <https://doi.org/10.5281/zenodo.6387882>.
38. A. Williams and D.B. Smith, The Combustion and Oxidation of Acetylene, *Chem. Rev.*, 1970, **70**(2), p 267–293.
39. Z. Liu, Z. Xing, H. Wang, X. Cui, G. Jin, and S. Chen, Fabrication and Post Heat Treatment of 0.5Pb(Mg1/3Nb2/3)O3-0.5Pb(Zr0.48Ti0.52)O3 Coatings by Supersonic Plasma Spray, *J. Eur. Ceram. Soc.*, 2017, **37**, p 3511–3519.
40. A.H. Pakseresht, M.R. Rahimpour, M.R. Vaezi, and M. Salehi, Effect of Splat Morphology on the Microstructure and Dielectric Properties of Plasma Sprayed Barium Titanate Films, *Appl. Surf. Sci.*, 2015, **324**, p 797–806.
41. L. Zhou, Z. Xing, H. Wang, P. He, Q. Mi, W. Guo, Y. Huang, L. Tang, H. Zhu, and X. Zhu, Interfacial Microstructure and Bonding Properties of Plasma-Sprayed Multilayer Ceramic Coating (Al<sub>2</sub>O<sub>3</sub>/BaTiO<sub>3</sub>/Al<sub>2</sub>O<sub>3</sub>-40 wt.% TiO<sub>2</sub>), *J. Therm. Spray Technol.*, 2020, **29**, p 2012–2025.
42. Y. Jiang, S.S. Mofarah, P. Koshy, W.F. Chen, X. Fang, X. Zheng, D. Wang, and C.C. Sorrell, Na<sub>0.5</sub>Bi<sub>0.5</sub>TiO<sub>3</sub> Phase Relations: Thermodynamics and Phase Equilibria in the Systems Bi<sub>2</sub>O<sub>3</sub>-TiO<sub>2</sub>, Na<sub>2</sub>O-TiO<sub>2</sub>, and Na<sub>2</sub>O-Bi<sub>2</sub>O<sub>3</sub>-TiO<sub>2</sub>, *J. Eur. Ceram. Soc.*, 2021, **41**(14), p 7005–7013.
43. D.A.H. Hanaor and C.C. Sorrell, Review of the Anatase to Rutile Phase Transformation, *J. Mater. Sci.*, 2011, **46**(4), p 855–874.
44. X. Zhao, H. Yang, S. Li, Z. Cui, and C. Zhang, Synthesis and Theoretical Study of Large-Sized Bi<sub>4</sub>Ti<sub>3</sub>O<sub>12</sub> Square Nanosheets with High Photocatalytic Activity, *Mater. Res. Bull.*, 2018, **107**, p 180–188.



45. J. Chen, C. Wang, C. Zong, S. Chen, P. Wang, and Q. Chen, High Catalytic Performance of Au/Bi<sub>2</sub>O<sub>3</sub> for Preferential Oxidation of CO in H<sub>2</sub>, *ACS Appl. Mater. Interfaces*, 2021, **13**(25), p 29532-29540.
46. M.C. Biesinger, L.W.M. Lau, A.R. Gerson, and R.S.C. Smart, Resolving Surface Chemical States in XPS Analysis of First Row Transition Metals, Oxides and Hydroxides: Sc, Ti, V, Cu and Zn, *Appl. Surf. Sci.*, 2010, **257**(3), p 887-898.
47. H. Idriss, On the Wrong Assignment of the XPS O1s Signal at 531-532 eV Attributed to Oxygen Vacancies in Photo- and Electro-Catalysts for Water Splitting and Other Materials Applications, *Surf. Sci.*, 2021, **712**, p 2-7.
48. M. Zeng, S.W. Or, and H.L.W. Chan, First-Principles Study on the Electronic and Optical Properties of Na<sub>0.5</sub>Bi<sub>0.5</sub>TiO<sub>3</sub> Lead-Free Piezoelectric Crystal, *J. Appl. Phys.*, 2010, **107**, p 043513.
49. P. Ctibor, V. Stengl, F. Zahalka, and N. Murafa, Microstructure and Performance of Titanium Oxide Coatings Sprayed by Oxygen-Acetylene Flame, 2011, (Iii), p 2-7.
50. J.A. Díaz-real, P. Elsaesser, T. Holm, and W. Mérida, Electrochemical Reduction on Nanostructured TiO<sub>2</sub> for Enhanced Photoelectrocatalytic Oxidation, *Electrochim. Acta*, 2019, **329**, p 135162.
51. J.A. Díaz-real, J. Ma, and N. Alonso-vante, Highly Photoactive Brookite and Anatase with Enhanced Photocatalytic Activity for the Degradation of Indigo Carmine Application, *Appl. Catal. B Environ.*, 2016, **198**, p 471-479. <https://doi.org/10.1016/j.apcatb.2016.06.008>
52. J. Van De Lagemaat and A.J. Frank, Nonthermalized Electron Transport in Dye-Sensitized Nanocrystalline TiO<sub>2</sub> Films: Transient Photocurrent and Random-Walk Modeling Studies, *J. Phys. Chem. B*, 2001, **105**, p 11194-11205.
53. M.E. Orazem, N. Pébère, and B. Tribollet, Enhanced Graphical Representation of Electrochemical Impedance Data, *J. Electrochem. Soc.*, 2006, **153**(4), p B129.
54. R. Beranek, (Photo) Electrochemical Methods for the Determination of the Band Edge Positions of TiO<sub>2</sub>-Based Nanomaterials, *Adv. Phys. Chem.*, 2011, p 80-83.

**Publisher's Note** Springer Nature remains neutral with regard to jurisdictional claims in published maps and institutional affiliations.

Springer Nature or its licensor (e.g. a society or other partner) holds exclusive rights to this article under a publishing agreement with the author(s) or other rightsholder(s); author self-archiving of the accepted manuscript version of this article is solely governed by the terms of such publishing agreement and applicable law.